ROYAL SOCIETY
OF CHEMISTRY

CrossMark
← click for updates

Oxygen etching of thick MoS$_2$ films

Robert Ionescu,[a] Aaron George,[b] Isaac Ruiz,[c] Zachary Favors,[b] Zafer Mutlu,[b]
Chueh Liu,[d] Kazi Ahmed,[c] Ryan Wu,[e] Jong S. Jeong,[e] Lauro Zavala,[f]
K. Andre Mkhoyan,[e] Mihri Ozkan[acd] and Cengiz S. Ozkan*[bf]

Oxygen annealing of thick MoS$_2$ films results in randomly oriented and controllable triangular etched shapes, forming pits with uniform etching angles. These etching morphologies differ across the sample based on the defect sites situated on the basal plane surface, forming numerous features in different bulk sample thicknesses.

2D Molybdenite (MoS$_2$) is an atomically thin transition-metal dichalcogenide that has emerged as a new material with great promise for applications in optoelectronics, nanoelectronics and spintronics.[1–3] MoS$_2$ has attracted a lot of attention with the analogous potential of graphene and its many applications.[4–7] Naturally found MoS$_2$ is a layered semiconductor material with a bandgap that ranges between 1.2–1.8 eV, depending on the number of layers.[1,2,8,9] Single layer MoS$_2$ is an excellent 2D material system for studying spintronics due to its broken inversion symmetry, which easily gives rise to coupling of spins and spin splitting in the valence band. MoS$_2$ has garnered significant attention due to the existence of a direct bandgap in the monolayer, which graphene's lack of has limited its applications.[1,3,10–12] Studies have shown that as the thickness of MoS$_2$ sheets decreases from bulk to monolayer, the electronic bandgap is converted from indirect to direct bandgap; which can be observed by changes in the photoluminescence (PL) and Raman signals.[9,13–20] Bulk MoS$_2$ is composed of van der Waals bonded S–Mo–S sheets. Each sheet is composed of a hexagonal plane of Mo atoms sandwiched in between two hexagonal planes of S atoms, which are held together by covalent bonds.[1,10,17,21,22]

The ability to etch thick films of MoS$_2$ to few layers or a single layer allows for control over properties such as the band gap and optical properties. Understanding the etching process of materials is essential to achieving such control and may also aid in understanding their functionalities, optical properties, and electronic properties. Control of the etching process parameters can produce various ordered structures and fascinating displays. It is known that the etching pattern of MoS$_2$ follows 120° or 60° between etched lines.[23,24] In this work, we report the first observations of constant angle etched CVD grown MoS$_2$, which reveals triangular, star, and hybrid etching patterns in a well-oriented manner by simple heating of the sample under oxygen-containing environment. We find that MoS$_2$ tends to etch triangular pits that follow the same etching angle and the same etching pattern.

MoS$_2$ films were grown on 300 nm thick SiO$_2$ by using an in-house thermal chemical vapor deposition (CVD) system. The samples were grown by ramping the system from room temperature to 500 °C in 1 hour and held for an additional hour at a pressure of 1–2 Torr, with a gas flow mixture of Ar/H$_2$ (4:1). This reaction converts the ammonium thiomolybdate precursor to MoS$_2$ in the presence of H$_2$.[25] Hydrogen in the first annealing step also reduces the amount of oxygen present in the tube. This process produced a MoS$_2$ film with a thickness of 10–20 nm, and is standard for growing such a material by CVD.[20–22,25] The MoS$_2$ sample was exposed to an Ar–O$_2$ mixture at a flow rate of 400 sccm, which initiates the etching process. After specified etching times, the furnace was cooled to room temperature under ambient conditions. The entire etching process is illustrated schematically in Fig. 1.

[a] *Department of Chemistry, University of California, Riverside, CA 92521, USA*

[b] *Materials Science and Engineering Program, University of California, CA 92521, USA*

[c] *Department of Electrical Engineering, University of California, CA 92521, USA*

[d] *Materials Science and Engineering Program, University of California, CA 92521, USA*

[e] *Department of Chemical Engineering and Materials Science, University of Minnesota, Minneapolis, MN 55455, USA*

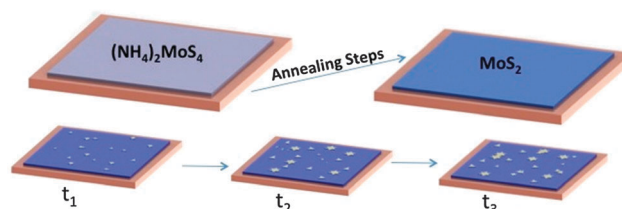[f] *Department of Mechanical Engineering, University of California, CA 92521, USA*
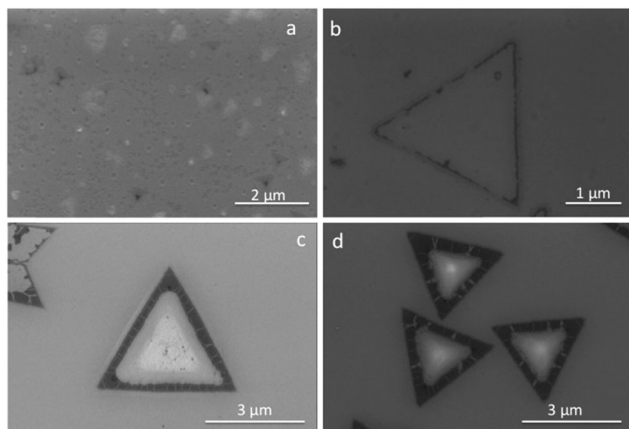
Fig. 1 Schematic of the growth to etching process.

Fig. 2 SEM images showing a time ordered evolution of etched patterns from (a–d) under the oxygen flow.
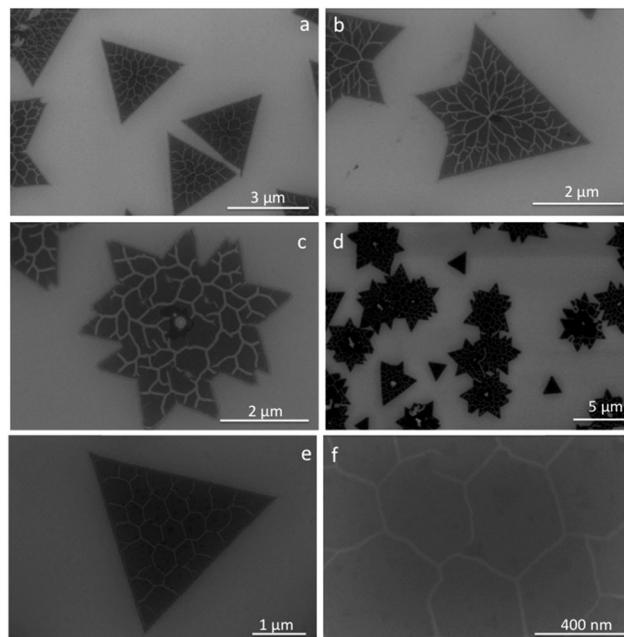
Fig. 3 SEM images of complete etched patterns (a–d) under the oxygen flow. In (e and f) single monolayer regions are observed on the bottom of the triangular pits.

As the etching process begins, triangular and star shaped etched morphologies become apparent and grow in size as exposure time is increased ($t_1 < t_2 < t_3$), as shown in Fig. 1. This oxidation etching effect can be prevented with the introduction of sulfur into the CVD chamber.

The etching morphology was characterized using a scanning electron microscope (SEM) (Leo-supra, 1550). Fig. 2d shows that the MoS_2 etching follows the same pattern of other published works on the growth of MoS_2, which follow triangular and star shaped morphologies.[21,22,26,27] The etching initiation appears as a small indentation on the oxidized surface of the film as shown by SEM in Fig. 2a. The initiation pits and triangular shape of the etched pits tend to come from extended lattice defects, such as edges or grain boundary mismatches between layers.[12,28–30] As the etching process continues, the pits grow and take the form of triangles and other geometric forms, which contain pseudo-hexagonal shaped branched nerves. The tendency for these symmetric patterns to form may be due to etching occurring along the preferential crystalline direction, a conclusion derived from our observation of numerous straight edged triangular shaped features.

As the etching initiates, as shown in Fig. 2, we see that the pits in different regions look like straight edge triangles with a contour around it. This can be observed in Fig. 3a–d, where depending on the different defect sites, we obtain various geometric shapes with the triangle being the most commonly seen with an average domain size of 3 μm. As time progresses, we observe MoS_2 etching at an angle forming an almost perfect pyramid structure in the middle, as seen in Fig. 2c and d. When enough time was allocated for the etching process, the pyramids disappeared, leaving behind a triangular pit. From Fig. 3a,[31,32] it is known that as the layers of MoS_2 increase, the interactions between the substrate and the material also increase, making the first MoS_2 layer more strongly bonded to the substrate.[33] This is a reasonable explanation for the presence of small triangles and the veins left on the bottom of the pits as seen in Fig. 3e and f. Extensive studies on graphene etching have shown that etching occurs along the preferential crystalline direction but with a high uncertainty due to randomness.[34–38] Etching veins start from the grain boundaries branching inward as seen in Fig. 2c and d to a point of origin of the grown crystals as observed in Fig. 3a–c. Depending on the etching rate along the lattice, the etching occurs in the regions that are most energetically favorable, leaving behind a vein-like network. Due to the etching effect, these veins like structures could very well come from residual stress. These reasonings explain the ordered loops formed in Fig. 2b and the hexagonally organized hexagonal features in Fig. 3e. These two-dimensional quasicrystalline or 'Penrose tilings' with six-fold symmetry look ordered but non-periodic. Based on previous research done on etching, it has been concluded that by taking into account the Eley–Rideal and Langmuir–Hinshelwood mechanism, MoS_2 thickness can alter the etching rate and the way oxygen reacts with the material.[23,39–41] The thickness and grain boundaries in CVD-prepared MoS_2 allow for the observation of these etching shapes, previously not seen in exfoliated samples. As previously discussed, due to different edge directions based on the layer orientation we could have different rates of etching yielding various shapes as seen in Fig. 3a–d. Having a higher than usual defect ratio, these sites of the sample tend to have an agglomeration of shapes forming star-like morphologies. These still follow the same etching angle pattern and similar features are seen as previously observed on the triangular regions.

Surface morphology and etching thicknesses were studied using an AFM (Veeco) under tapping mode imaging. As seen in the AFM images, the triangular shape pits resemble the lattice of the MoS_2 basal plane surface with the edge along the zigzag direction having a lattice terminating in either Mo or S. Raman spectra taken using a Horiba LabRAM HR spectrometer with an excitation wavelength of 532 nm was used to determine the number of MoS_2 layers, but this can also be easily calculated from the AFM height profile. We can clearly see in Fig. 4a that the color scheme changes across the sample, pointing out that the sample has a wavy trend due to the
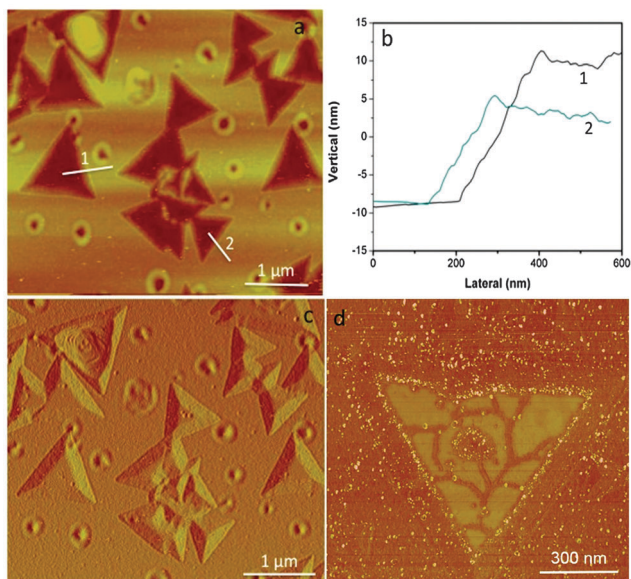
Fig. 4 AFM images (a), (c) and (d) of etched pits along with height profile in (b) of the MoS_2 pits.

Fig. 5 Molecular Schematic of (a) Mo edge and (b) S edge. (c) A filtered high resolution TEM image of an MoS_2 sample.

substrate and film preparation.[42] This is an advantage since we can see what happens to the etching pattern in the film at different levels of thickness. In Fig. 4c we observe and validate that the triangles are in fact etching down into the film and the veins observed in the SEM images are illustrated in Fig. 4d. Despite the fact that it has previously been reported that it is difficult to obtain AFM height profiles of thick MoS_2 layers,[23] we have successfully obtained such measurements with our grown MoS_2 films as seen in Fig. 4b. Taking into consideration the variations of film thickness across our samples, we deduce that the film has regions in between 10–20 nm, which can clearly be seen in our AFM height profile. It is known that the surface roughness of the under layer substrate affects the thickness of layer.[43] We report in this work, for the first time, the etching angle calculated from the height profile measurement. We report the etching angle to be 85 degrees normal to the wafer and constant across all samples. We can see that for both etched pits at 10 nm and 20 nm it follows the same etching angle all the way down to the substrate. We assume that this angle, just like the shape of the etched pits, comes from the lattice structure out of the material.

Mo atoms are coordinated to six S atoms, and become saturated with S in the bulk form of MoS_2. Density functional theory (DFT) calculations have shown that structures with one S atom per Mo edge atom results in S atoms at the edge.[28,44,45] In other cases where two S atoms per Mo edge are present, the structure will have a Mo edge.[28,44,45] Looking at the MoS_2 structure we see a hexagonal layered lattice (Fig. 5a–c) just as seen in graphene. Raw transmission electron microscopy (TEM) image in Fig. 5c was taken using an FEI Titan G^2 60–300 aberration-corrected TEM operating at 200 keV. Low pass and radial image filters were subsequently used to accentuate atomic positions. TEM confirms this hexagonal MoS_2 structure as shown in Fig. 5c where the higher intensity positions are Mo atoms and the lower intensity positions are S atoms. Furthermore, the image also confirms that the film is $2H$-MoS_2 based on the relative intensity ratio of the two atomic positions.[46,47]
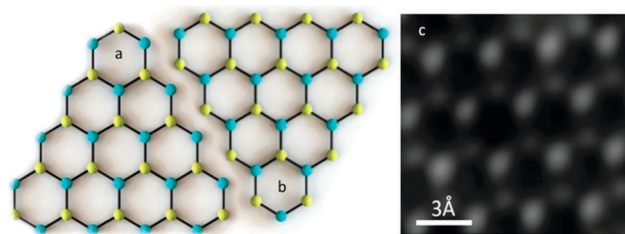
MoS_2 is yet unique considering that one layer is composed of three individual atomic layers where Mo layers are sandwiched between two S layers, giving a zigzag three-atom layer rather than a one-atom layer of carbon known as graphene. Taking this in consideration we can now say that the MoS_2 basal plane surface has a triangular shape. The MoS_2 edge structure is known to be represented by either Mo-terminated zigzag (ZZ-Mo) or S_2-terminated zigzag (ZZ-S_2), both illustrated in Fig. 5a and b.[28–30] By knowing this, the edges of the layer forming the pits are either ZZ-Mo or ZZ-S_2 edge. These microscale pits described earlier can act as seeds across the surface and the zigzag edges will grow when a reaction starts from a surface vacancy.[36,37] Evidence from other studies suggests that the Mo-edge is in fact more energetically stable and thus, more favored than the S edge.[48,49] We know that the triangular pit sizes are dependent on the number of layers of MoS_2; the more layers there are, the bigger the pit sizes and the lower the etching rate on the MoS_2 surface.[23] Since our study is based on oxygen etching, it has been previously reported that due to structural defects, etching is likely to happen at those sites. This notion tends to imply that etching strongly depends on the crystallographic orientation, which results in the zigzag formations.[23] The Mo and S atoms found at the edge are converted to MoO_3 and SO_2 gas molecules at higher temperatures.[23,50,51] If the etching starts from a ZZ-Mo edge, the oxygen reacts first with Mo and then S, but if the etching starts with a ZZ-S_2, then we have a reaction with S first and then with Mo.[23,24,48,49] It has been reported in previous studies that ZZ-Mo triangles have sharper and straighter edges than ZZ-S_2 triangles.[21] Knowing this we concluded that our material edges are in fact ZZ-Mo edge illustrated in Fig. 5a.

Raman spectroscopy measurements were carried out using a Renishaw DXR Raman spectroscopy system with a 532 nm laser (8 mW excitation power, 100× objective lens) and used to characterize the layers, quality, and etching of the MoS_2 film. In Fig. 6a
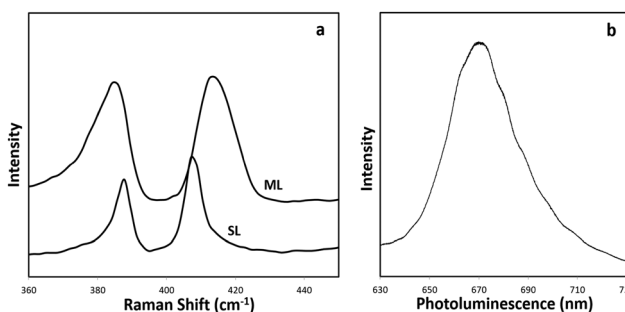

Fig. 6 In (a) we see the Raman spectra of multi-layer (ML) MoS_2 and single layer (SL) MoS_2 along with the photoluminescence in (b).

the domains clearly demonstrate the characteristic Raman peaks of E_{2g} and A_{1g}, from single and bulk MoS_2 film.[21,52] Raman E_{2g} mode at 386 cm^{-1} and A_{1g} mode at 405 cm^{-1} correspond to a monolayer MoS_2 which is found on the bottom of the pits as seen in the SEM Fig. 3e. Raman E_{2g} mode at 384 cm^{-1} and A_{1g} mode at 414 cm^{-1} correspond to bulk MoS_2 prior to oxidation due to the film being 10–20 nm thick. PL of these samples was taken and recorded to have a noticeable intensity only inside the wells. The PL spectra seen in Fig. 6b was recorded at 670.5 nm translating to about 1.85 eV, which has previously been reported in literature as monolayer regions. The high PL intensity, which has been previously reported, is known to come from the decrease of electron density resulting from sulfur-rich defect states after etching.[20–23,25,30,53] In both Raman and PL spectra, a peak located at 521 cm^{-1} in the spectrum was observed, corresponding to the Si–SiO$_2$ substrate. The measurements provide evidence of the MoS_2 etching and the fact that a longer etching time (20–30 min) leads to the complete removal of the MoS_2 film spanning a high intensity Si peak. After etching, the presence of MoO_3 was not observed by Raman spectroscopy, in accordance with previous studies.[23]

In summary, we report on the etching of thick MoS_2 films with well-oriented etching patterned pits of different morphologies. Etching pits were obtained by exposing the MoS_2 film to oxygen flow. Similar etching angles were observed to be constant across the sample along with veins and minuscule triangles features. We conclude that the etching effects initiate on the MoS_2 films rather than substrate, but the substrate plays a role in the etching of the MoS_2 layer in contact with the Si–SiO$_2$ substrate.

Notes and references

1 B. Radisavljevic, A. Radenovic, J. Brivio, V. Giacometti and A. Kis, *Nat. Nanotechnol.*, 2011, **6**, 147–150.
2 J. Yoon, W. Park, G.-Y. Bae, Y. Kim, H. S. Jang, Y. Hyun, S. K. Lim, Y. H. Kahng, W.-K. Hong, B. H. Lee and H. C. Ko, *Small*, 2013, 3295–3300.
3 Q. H. Wang, K. Kalantar-Zadeh, A. Kis, J. N. Coleman and M. S. Strano, *Nat. Nanotechnol.*, 2012, **7**, 699–712.
4 J. R. Kyle, A. Guvenc, W. Wang, M. Ghazinejad, J. Lin, S. Guo, C. S. Ozkan and M. Ozkan, *Small*, 2011, **7**, 2599–2606.
5 S. Guo, M. Ghazinejad, X. Qin, H. Sun, W. Wang, F. Zaera, M. Ozkan and C. S. Ozkan, *Small*, 2012, **8**, 1073–1080.
6 W. Wang, S. Guo, M. Penchev, I. Ruiz, K. N. Bozhilov, D. Yan, M. Ozkan and C. S. Ozkan, *Nano Energy*, 2013, **2**, 294–303.
7 Q. Yu, L. A. Jauregui, W. Wu, R. Colby, J. Tian, Z. Su, H. Cao, Z. Liu, D. Pandey, D. Wei, T. F. Chung, P. Peng, N. P. Guisinger, E. A. Stach, J. Bao, S.-S. Pei and Y. P. Chen, *Nat. Mater.*, 2011, **10**, 443–449.
8 S. Lei, L. Ge, Z. Liu, S. Najmaei, G. Shi, G. You, J. Lou, R. Vajtai and P. M. Ajayan, *Nano Lett.*, 2013, **13**, 2777–2781.
9 J. K. Ellis, M. J. Lucero and G. E. Scuseria, *Appl. Phys. Lett.*, 2011, **99**, 261908.
10 K. F. Mak, C. Lee, J. Hone, J. Shan and T. F. Heinz, *Phys. Rev. Lett.*, 2010, **105**, 136805.
11 A. K. Geim and K. S. Novoselov, *Nat. Mater.*, 2007, **6**, 183–191.
12 A. H. Castro Neto, N. M. R. Peres, K. S. Novoselov and A. K. Geim, *Rev. Mod. Phys.*, 2009, **81**, 109–162.
13 M. Valden, *Science*, 1998, **281**, 1647–1650.
14 Y. Guo, *Science*, 2004, **306**, 1915–1917.
15 L.-Y. Ma, L. Tang, Z.-L. Guan, K. He, K. An, X.-C. Ma, J.-F. Jia, Q.-K. Xue, Y. Han, S. Huang and F. Liu, *Phys. Rev. Lett.*, 2006, **97**, 266102.
16 X. Ma, P. Jiang, Y. Qi, J. Jia, Y. Yang, W. Duan, W.-X. Li, X. Bao, S. B. Zhang and Q.-K. Xue, *Proc. Natl. Acad. Sci. U. S. A.*, 2007, **104**, 9204–9208.
17 A. Splendiani, L. Sun, Y. Zhang, T. Li, J. Kim, C.-Y. Chim, G. Galli and F. Wang, *Nano Lett.*, 2010, **10**, 1271–1275.
18 C. Lee, H. Yan, L. E. Brus, T. F. Heinz, J. Hone and S. Ryu, *ACS Nano*, 2010, **4**, 2695–2700.
19 Y. Wang, C. Cong, C. Qiu and T. Yu, *Small*, 2013, **9**, 2857–2861.
20 Y. Zhan, Z. Liu, S. Najmaei, P. M. Ajayan and J. Lou, *Small*, 2012, **8**, 966–971.
21 A. M. van der Zande, P. Y. Huang, D. A. Chenet, T. C. Berkelbach, Y. You, G.-H. Lee, T. F. Heinz, D. R. Reichman, D. A. Muller and J. C. Hone, *Nat. Mater.*, 2013, **12**, 554–561.
22 S. Najmaei, Z. Liu, W. Zhou, X. Zou, G. Shi, S. Lei, B. I. Yakobson, J.-C. Idrobo, P. M. Ajayan and J. Lou, *Nat. Mater.*, 2013, **12**, 754–759.
23 H. Zhou, F. Yu, Y. Liu, X. Zou, C. Cong, C. Qiu, T. Yu, Z. Yan, X. Shen, L. Sun, B. I. Yakobson and J. M. Tour, *Nano Res.*, 2013, **6**, 703–711.
24 M. Yamamoto, T. L. Einstein, M. S. Fuhrer and W. G. Cullen, *J. Phys. Chem. C*, 2013, **117**, 25643–25649.
25 K.-K. Liu, W. Zhang, Y.-H. Lee, Y.-C. Lin, M.-T. Chang, C.-Y. Su, C.-S. Chang, H. Li, Y. Shi, H. Zhang, C.-S. Lai and L.-J. Li, *Nano Lett.*, 2012, **12**, 1538–1544.
26 S. Wu, C. Huang, G. Aivazian, J. S. Ross, D. H. Cobden and X. Xu, *ACS Nano*, 2013, **7**, 2768–2772.
27 R. Ionescu, W. Wang, Y. Chai, Z. Mutlu, I. Ruiz, Z. Favors, D. Wickramaratne, M. Neupane, L. Zavala, R. Lake, M. Ozkan and C. Ozkan, *IEEE Trans. Nanotechnol.*, 2014, 1.
28 S. Helveg, J. Lauritsen, E. Lægsgaard, I. Stensgaard, J. Nørskov, B. Clausen, H. Topsøe and F. Besenbacher, *Phys. Rev. Lett.*, 2000, **84**, 951–954.
29 T. F. Jaramillo, K. P. Jorgensen, J. Bonde, J. H. Nielsen, S. Horch and I. Chorkendorff, *Science*, 2007, **317**, 100–102.
30 H. Schweiger, *J. Catal.*, 2002, **207**, 76–87.
31 J. Wu, H. Li, Z. Yin, H. Li, J. Liu, X. Cao, Q. Zhang and H. Zhang, *Small*, 2013, 3314–3319.
32 A. Castellanos-Gomez, M. Barkelid, A. M. Goossens, V. E. Calado, H. S. J. van der Zant and G. A. Steele, *Nano Lett.*, 2012, **12**, 3187–3192.
33 D. Le, D. Sun, W. Lu, L. Bartels and T. S. Rahman, *Phys. Rev. B: Condens. Matter Mater. Phys.*, 2012, **85**, 075429.
34 D. Geng, B. Wu, Y. Guo, B. Luo, Y. Xue, J. Chen, G. Yu and Y. Liu, *J. Am. Chem. Soc.*, 2013, **135**, 6431–6434.
35 B. Wu, D. Geng, Z. Xu, Y. Guo, L. Huang, Y. Xue, J. Chen, G. Yu and Y. Liu, *NPG Asia Mater.*, 2013, **5**, e36.
36 R. Yang, L. Zhang, Y. Wang, Z. Shi, D. Shi, H. Gao, E. Wang and G. Zhang, *Adv. Mater.*, 2010, **22**, 4014–4019.
37 Z. Shi, R. Yang, L. Zhang, Y. Wang, D. Liu, D. Shi, E. Wang and G. Zhang, *Adv. Mater.*, 2011, **23**, 3061–3065.
38 G. Xie, Z. Shi, R. Yang, D. Liu, W. Yang, M. Cheng, D. Wang, D. Shi and G. Zhang, *Nano Lett.*, 2012, **12**, 4642–4646.
39 R. T. Yang, *J. Chem. Phys.*, 1981, **75**, 4471.
40 H. Chang and A. J. Bard, *J. Am. Chem. Soc.*, 1990, **112**, 4598–4599.
41 J. R. Hahn, H. Kang, S. M. Lee and Y. H. Lee, *J. Phys. Chem. B*, 1999, **103**, 9944–9951.
42 J. Brivio, D. T. L. Alexander and A. Kis, *Nano Lett.*, 2011, **11**, 5148–5153.
43 H. R. Gutiérrez, N. Perea-López, A. L. Elías, A. Berkdemir, B. Wang, R. Lv, F. López-Urías, V. H. Crespi, H. Terrones and M. Terrones, *Nano Lett.*, 2013, **13**, 3447–3454.
44 L. Byskov, *J. Catal.*, 1999, **187**, 109–122.
45 P. Raybaud, J. Hafner, G. Kresse and H. Toulhoat, *Surf. Sci.*, 1998, **407**, 237–250.
46 R. J. Wu, M. L. Odlyzko and K. A. Mkhoyan, *Ultramicroscopy*, 2014, **147**, 8–20.
47 G. Eda, T. Fujita, H. Yamaguchi, D. Voiry, M. Chen and M. Chhowalla, *ACS Nano*, 2012, **6**, 7311–7317.
48 J. V. Lauritsen, J. Kibsgaard, S. Helveg, H. Topsøe, B. S. Clausen, E. Lægsgaard and F. Besenbacher, *Nat. Nanotechnol.*, 2007, **2**, 53–58.
49 L. S. Byskov, J. K. Nørskov, B. S. Clausen and H. Topsøe, *Catal. Lett.*, 1999, **64**, 95–99.
50 S. Ross and A. Sussman, *J. Phys. Chem.*, 1955, **59**, 889–892.
51 J. R. Lince and P. P. Frantz, *Tribol. Lett.*, 2000, **9**, 211–218.
52 B. Chakraborty, H. S. S. R. Matte, A. K. Sood and C. N. R. Rao, *J. Raman Spectrosc.*, 2013, **44**, 92–96.
53 K. F. Mak, K. He, C. Lee, G. H. Lee, J. Hone, T. F. Heinz and J. Shan, *Nat. Mater.*, 2012, **12**, 207–211.